Sputtered iridium oxide film (SIROF) for on-chip microsupercapacitors with integrated solar charging

Journal of Energy Storage 161 (2026) 121720

Contents lists available at ScienceDirect

Journal of Energy Storage

journal homepage: www.elsevier.com/locate/est

Research papers

Sputtered iridium oxide film (SIROF) for on-chip microsupercapacitors with integrated solar charging

Qi Li [a,*], Lukas Matter [b], Muhammad Hassan [b], R.K. Azega [b], Hanna Karlsson-Fernberg [b], Björn Wickman [c], Johan Liu [b], Maria Asplund [b], Per Lundgren [b], Mazharul Haque [c,*]

[a] Independent Researcher, Gothenburg, Sweden
[b] Electronics Material and Systems, Department of Microtechnology and Nanoscience, Chalmers University of Technology, Gothenburg, Sweden
[c] Chemical Physics, Department of Physics, Chalmers University of Technology, Gothenburg, Sweden

ARTICLE INFO

Keywords:
Iridium oxide
Pseudocapacitance
EDLC
Ionic liquid
Aqueous electrolyte
Gel electrolyte
Microsupercapacitor

ABSTRACT

The rapid development of microsupercapacitors (MSCs) has increased demand for high-performance electrode materials that can provide long-lasting energy storage with high power and energy densities. Sputtered iridium oxide film (SIROF) is a promising option due to its superior pseudocapacitive behavior, scalability, and compatibility with microfabrication techniques. In this work, we have explored sputtered iridium oxide films (SIROF) with a platelet morphology as electrode materials for on-chip microsupercapacitors. The electrochemical performance of the devices is systematically evaluated in a variety of electrolytes including acidic, neutral, alkaline, gel, and ionic liquid systems. Among aqueous electrolytes phosphoric acid (H_3PO_4) delivers the highest areal capacitance of 48.6 mF cm^{-2}. The PVA/H_3PO_4 gel electrolyte provides enhanced cycling stability, retaining 99.5% of its capacitance after 10,000 cycles and exhibits reduced self-discharge. The ionic liquid EMIM TFSI enables higher energy and power densities through an extended operating voltage window and stable operation at elevated temperature of 60 °C. These findings provide valuable insights into the impact of electrode/electrolyte interaction on the overall performance of SIROF. Additionally, the MSCs demonstrate scalable operation and can be efficiently charged using commercial photovoltaic cells, highlighting their potential for integration into self-powered microelectronic systems. These results highlight the versatility of SIROF electrodes and their suitability for next-generation micro-energy storage applications.

1. Introduction

The increasing demand for efficient, miniaturized energy storage solutions has driven considerable interest in microsupercapacitors (MSCs), owing to their high-power density, rapid charge–discharge rates, and extended cycle life [1]. Unlike conventional supercapacitors, MSCs offer seamless integration with microelectronic systems, making them ideal for powering compact devices such as wearable electronics, Internet of Things (IoT), sensors, and implantable biomedical devices [2]. Despite significant advances in device architectures the achievable energy and power densities of MSCs remain strongly constrained by the choice of electrode materials, electrolyte composition, and the interfacial interactions between them.

Various electrode materials for MSCs have been investigated, including carbon-based materials (e.g., graphene, carbon nanotubes, activated carbon) [3], transition metal oxides (e.g., ruthenium oxide (RuO_2), manganese oxide (MnO_2), nickel oxide (NiO)) [4], and conducting polymers (e.g., polyaniline, polypyrrole) [5], each exhibiting distinct advantages and limitations. Carbon-based electrodes generally exhibit excellent cyclic stability but suffer from relatively low energy density, whereas conducting polymers provide higher energy densities at the expense of reduced cycle life [6]. Transition metal oxides represent a compelling alternative, owing to their intrinsic pseudocapacitive behavior, which enables higher energy densities than carbon-based materials while offering improved stability relative to conducting polymers [6].

Among different metal oxides, iridium oxide (IrO_x) has emerged as a promising candidate for MSCs due to its excellent electrical conductivity, wide electrochemical stability window, and rich redox chemistry [7–9]. Beyond its application in energy storage systems [10], IrO_x has demonstrated utility in neural stimulation devices [11,12], piezoelectric and pyroelectric sensors [13], and electrolysis processes [14]. The

* Corresponding authors.
E-mail addresses: qili.energy@hotmail.com (Q. Li), mhaque@chalmers.se (M. Haque).

https://doi.org/10.1016/j.est.2026.121720
Received 29 September 2025; Received in revised form 7 February 2026; Accepted 21 March 2026
Available online 3 April 2026

physical and chemical properties of IrO_x are significantly influenced by their shape, morphology and surface chemistry [9]. Reactive sputtering is a synthesis technique that enables precise control over oxygen pressure, power, and substrate temperature [13,15,16], yielding sputtered iridium oxide films (SIROFs) with tunable thickness and surface structure. Platelet-like morphologies, in particular, offer high porosity and large electrochemically active surface area, which are expected to enhance electrochemical performance compared to conventional dense film structures [16].

In addition, on-chip integration of MSCs with other components in a microelectronic device is very critical. In this context, SIROFs offer a distinct advantage due to their inherent compatibility with complementary metal oxide semiconductor (CMOS) processing and standard microfabrication techniques [17,18]. Unlike many carbon- or graphene-based electrodes that require high-temperature annealing or aggressive post-treatments [19], SIROFs can be deposited by sputtering at relatively low temperatures with excellent film adhesion. This enables integration with temperature-sensitive components, such as energy harvesters [20], as shown in Fig. S1, without disrupting established fabrication process flows [13,15,16]. Regardless of these advantages the electrochemical performance of SIROF-based MSCs has not been systematically evaluated across a broad range of electrolyte systems. To date, most studies have focused on its performance in biomimicking electrolyte, phosphate-buffered saline (PBS), leveraging its charge-injection capability, and biocompatibility [11,21–23]. Therefore current understanding of the performance of SIROF-based MSCs is largely restricted to a narrow range of electrolytes [7,24,25] and does not capture its full potential for micro-energy storage applications.

Electrolyte selection plays a decisive role in MSC performance by governing ionic transport, interfacial charge transfer, electrochemical stability, and long-term reliability [26,27]. Aqueous electrolytes are attractive due to their high ionic conductivity, low cost, and safety. However, their narrow electrochemical window (1.23 V) limits energy output and can lead to gas evolution and electrode degradation, especially in acidic media [28,29]. Organic electrolytes extend the operational voltage window (up to 2.7 V) but suffer from flammability, toxicity, and reduced ionic mobility at room temperature, which hinders safe and efficient operation [30]. Ionic liquids (ILs) offer a promising alternative due to their wide electrochemical stability, non-volatility, and excellent thermal resilience [31–34]. Nevertheless, their widespread adoption is constrained by high viscosity, synthesis complexity, and relatively low conductivity at ambient conditions [35]. Gel polymer electrolytes serve as an intermediate solution, offering enhanced mechanical stability and safety, although often at the cost of reduced ionic transport [36,37]. How SIROF electrodes respond to these fundamentally different electrolyte environments and how electrolyte choice mediates the balance between different charge storage mechanisms that defines the overall device performance remains largely unexplored.

To address these aspects, this study provides a comprehensive evaluation of SIROF-based MSCs across a broad spectrum of electrolytes, including acidic (H_2SO_4, H_3PO_4), neutral (Na_2SO_4, PBS), alkaline (NaOH), gel polymer (PVA/H_3PO_4), and ionic liquid (EMIM TFSI) systems. Electrochemical characterization techniques such as cyclic voltammetry (CV), galvanostatic charge–discharge (GCD), and electrochemical impedance spectroscopy (EIS) are employed to quantify specific capacitance, impedance characteristics, rate capability, and coulombic efficiency over a range of scan rates and current densities. Among the systems evaluated, H_3PO_4-based electrolytes exhibit the highest areal capacitance of 48.6 mF cm^{-2} and dominant capacitive behavior originating from electrical double layer (EDL) capacitance and pseudocapacitance, while PVA/H_3PO_4 gel electrolytes offer great scalability in terms of voltage and capacitance modulation with series and parallel connection and around 8% reduced self-discharge compared to the liquid counterpart. Notably, the use of EMIM TFSI ionic liquid enables the highest energy and power densities attributed to its broader electrochemical stability window up to 2 V. By directly comparing electrolyte-dependent charge storage mechanisms and device performance, this study establishes design guidelines for optimizing SIROF-based MSCs and demonstrates their potential as scalable, integrable electrode material for high-performance microscale energy storage applications.

2. Experimental

2.1. SIROF deposition and MSC fabrication

The fabrication process of the SIROF-based MSCs is illustrated in Fig. 1(a). A 4-inch oxidized silicon wafer with a thermally grown SiO_2 layer (thickness: 400 nm) was employed as the substrate (Step a1). Standard photolithography techniques were utilized to define the interdigital electrode patterns (Steps a2–a4), as depicted in Fig. 1(b).

To form the MSC pattern Fig. 1(b), the substrate was initially spin-coated with LOR3A at 2000 rpm for 60s followed by 5 mins bake at 150 °C, and afterwards S1813 photoresists (PR) was spin-coated at 3000 rpm for 60s followed by 100 s bake at 100 °C. Patterning was performed using a laser writer (MLA150), followed by development in MF CD-26 developer to expose the areas designated for metal deposition (Step a2). A titanium (Ti) adhesion layer (10 nm) and a platinum (Pt) current collector layer (150 nm) were then deposited sequentially via electron-beam evaporation (Lesker PVD 225). Afterwards, Iridium (Ir) and iridium oxide (IrO_x) thin films were deposited using a Nordiko 2000 sputtering system (Nordiko Technical Service Ltd., United Kingdom) under a process pressure of 17 mTorr and a DC power of 100 W. The target-to-substrate distance was set to 80 mm. Ir was initially sputtered for 1 min in an argon (Ar) atmosphere with a flow rate of 26 sccm. Subsequently, oxygen (O_2) was introduced at a flow rate of 14 sccm to initiate IrO_x deposition, which continued for 10 min (Step a3). The final device structure was realized via a lift-off process where the wafer was immersed in a vertical beaker filled with mr REM-400 remover and sonicated for around 10 mins (Step a4). Afterwards, the wafer was diced with a dicing saw (Disco DAD3350) to obtain individual MSCs. The geometrical parameters of the fabricated MSCs are summarized in Table 1.

2.2. Film thickness

To determine the film thickness, six strips of adhesive tape were randomly placed on a 4-inch silicon wafer before deposition to serve as masking regions. After the sputtering process and tape removal, the step height or thickness of the deposited Ir/IrO_x layers was measured using a profilometer (Tencor AS500, Tencor Instruments, USA). The average thickness of the deposited film was found to be 649 ± 64 nm.

2.3. Reservoir fabrication

For long-term cycling tests, the MSCs were placed into reservoirs and sealed with a lid to prevent electrolyte evaporation. Rectangular reservoirs (12 × 7.6 mm^2) with a height of 5 mm and a wall thickness of 500 μm were 3D printed (Form 3B+, Formlabs Inc., United States) using a resin (RS-F2-GPGR-04, Formlabs Inc.). The reservoirs were attached to microscope slides using a silicone paste (Sylgard 184, Dow, United States). The silicone paste was cured on a hot plate for 3 h at 80 °C. The reservoirs had a cutout at the bottom for the devices to slide into. After aligning the device and connecting wires to the contact pads outside of the reservoirs with a silver paste, the cutout was sealed with silicone paste and cured. A picture of the MSC with a reservoir is shown in Fig. 1 (c).

2.4. PVA/H_3PO_4 gel electrolyte preparation

The PVA/H_3PO_4 gel electrolyte was prepared by dissolving 1 g polyvinyl alcohol (PVA) (Sigma-Aldrich) in 10 mL deionized water at

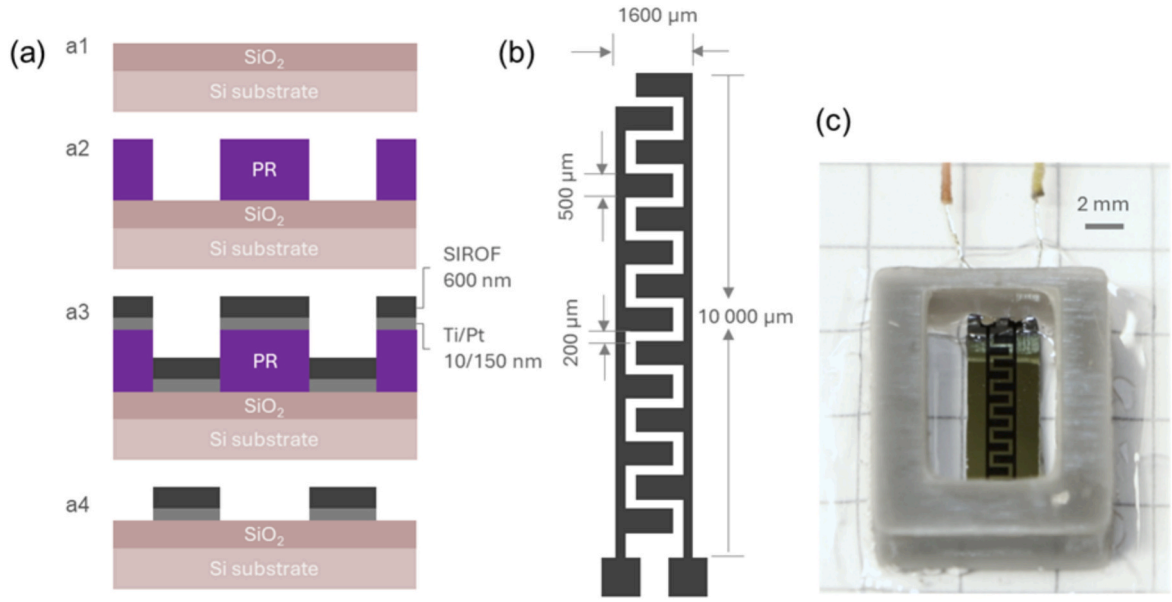

Fig. 1. SIROF-based MSCs: (a) Fabrication process steps, (b) Schematic illustration of the device configuration, (c) Photograph of a device enclosed in a 3D printed reservoir for measurements with liquid electrolytes.

Table 1
MSC total and active area.

Total device area, A_{total}	0.16 cm^2
Active SIROF area, A_{active}	0.11 cm^2
Active area ratio, A_{active}/ A_{total}	68.8%

55–60 °C water bath under continuous stirring until a clear, viscous solution was obtained. After cooling to approximately 30–35 °C, 1 mL H_3PO_4 (85 wt% solution, Sigma-Aldrich) was gradually added to the PVA solution, with constant stirring to ensure homogeneity. The resulting mixture formed a clear, flexible gel upon cooling to room temperature, as shown in Fig. S2.

2.5. Electrochemical characterizations

Cyclic voltammetry (CV) of MSCs was performed at scan rates ranging from 5 to 5000 mV s^{-1}. For quantifying the materials properties, the capacitance densities of single SIROF electrode $C_{A,SIROF}$, were extracted from the average of anodic and cathodic scans, and were normalized to the active SIROF area A_{active} (total geometric area of two electrodes), i.e., excluding the area of the spaces between the interdigital electrode fingers, as shown in Eq. (1):

$$C_{A,SIROF}\left(mF\mathrm{cm}^{-2}_{SIROF}\right) = 4 \times \frac{\int idV}{2 \times \nu \bullet \Delta V} \bullet \frac{1}{A_{active}} \tag{1}$$

where i (mA) is the measured current, ν (V s^{-1}) is the scan rate, and ΔV (V) is the voltage window.

For galvanostatic charge-discharge (GCD) characterization, the devices were measured in a voltage window of 0 to 0.8 V, at current densities from 10 to 1000 µA cm^{-2}. The current densities were normalized to the total MSC device area, A_{total}. The MSC device capacitance density is calculated according to Eq. (2):

$$C_{A,Device}\left(mF\ cm^{-2}_{Device}\right) = \frac{i \bullet \Delta t}{1000 \bullet \Delta V} \bullet \frac{1}{A_{active}} \tag{2}$$

swhere i (mA) is the constant current, Δt (s) is the discharge time, and ΔV (V) is the discharge voltage window excluding IR drop.

Volumetric capacitance density (e.g. $C_{V,\ SIROF}$, $C_{V,\ Device}$) is calculated by dividing the areal capacitance values by the film thickness.

The energy and power densities are calculated from GCD curves based on the following equations:

$$E_A\left(J\ \mathrm{cm}^{-2}_{\mathrm{Device}}\right) = \frac{1}{2} C_{A,Device} \bullet \Delta V^2 \tag{3}$$

$$P_A\left(W\ \mathrm{cm}^{-2}_{\mathrm{Device}}\right) = \frac{E_A}{\Delta t} \tag{4}$$

$$E_V\left(J\ \mathrm{cm}^{-3}_{\mathrm{Device}}\right) = \frac{1}{2} \frac{C_{A,Device}}{d_{film}} \bullet \Delta V^2 \tag{5}$$

$$P_V\left(W\ \mathrm{cm}^{-3}_{\mathrm{Device}}\right) = \frac{E_V}{\Delta t} \tag{6}$$

where E_A and P_A represent areal energy and power densities. The film thickness is denoted as d_{film} (649 nm, i.e. 649 × 10^{-7} cm), to calculate the volumetric energy E_V and power densities P_V from their areal values.

Electrochemical impedance spectroscopy (EIS) has been carried out at a frequency range of 100 kHz to 10 mHz at 0 V with an alternating current (ac) perturbation of 10 mV at open circuit potential.

Open circuit potential measurements were conducted in all fabricated devices including those units configured in series and parallel. Out of 114 devices on a single wafer (Fig. S3), 107 were found to be functional. Afterwards, the successfully encapsulated devices with electrolytes were subjected to electrochemical measurements. A complete set of electrochemical measurements such as (CV, GCD, EIS, Self-discharge, and cycling stability test) were conducted on a single device with the representative electrolyte. All electrochemical measurements were conducted using a Gamry Reference 3000AE Galvanostat/potentiostat workstation with an electrometer input impedance of >1014 Ω, current accuracy of (± 1 mV, ±0.3%) reading. The measurements were carried out at room temperature (RT), 21 °C, besides a part of the measurements with EMIM TFSI electrolyte, which were conducted at an elevated temperature of 60 °C. Elevated temperature was achieved by placing the device in a DZF-6020 oven (temperature fluctuation ±1 °C). Additionally, the temperature was monitored by a UT61B modern digital multimeter coupled with a thermal sensor connected to the device. The accuracy of the sensor is ±1.2% in a temperature range of −40 to 1000 °C. Once the device reached the pre-set temperature, it was maintained at that constant temperature for at least 4 h to ensure that the critical dynamical processes could reach thermal equilibrium before

the test.

2.6. Materials characterizations

The morphology of SIROF was studied by using a scanning electron microscope (SEM, JEOL 7800F Prime) in a secondary electron mode at an acceleration voltage of 5 kV. X-ray photoelectron spectroscopy (XPS) measurements were conducted on PHI 5000 Versa Probe system equipped with a monochromatic Al Kα X-ray (E = 1486.6 eV) source with beam size diameter of 100 μm. The charging shift was calibrated using the C 1 s photoemission line at a binding energy of 284.8 eV. High-resolution spectra of Ir 4f (58.75–69.75 eV, 111 points) and O 1 s (526.15–538.15 eV, 121 points) core-levels were acquired with 0.1 eV step size. Background subtraction was performed using the Shirley algorithm. Peak areas were integrated using numerical trapezoid integration of the net spectrum (raw minus background). The Ir:O atomic ratio was determined using published Scofield relative sensitivity factors (RSF): RSF (Ir 4f) = 14.33, RSF (O 1 s) = 2.85 [38]. X-ray diffraction (XRD) pattern was collected using a Bruker D8 Discover X-ray diffractometer and analysis was performed using Cu Kα radiation (λ = 1.54184 Å) at a scan rate of 1.5° min^{-1}. The resistivity of SIROF was measured with a four-probe semi-automated sheet resistance and resistivity measurement system (CMT-SR2000N, Switzerland).

3. Results and discussion

3.1. Material properties

High-resolution images of fabricated SIROF are shown in Fig. 2(a-c). The SIROF shows a typical platelet structure, with individual platelets of approximately sub 10 nm thickness. The formation mechanism of platelet SIROF can vary based on the sputtering parameters and substrate used. Deposition of platelet SIROF is enabled by the formation of gas-phase clusters at sufficiently high oxygen flow rates, which lead to shadowing and the growth along the preferred (110) direction [39].

The crystal structure as well as the compositions of the sputtered SIROF are determined by XRD and XPS characterizations, respectively. The XRD pattern in Fig. 3(a) suggests that the SIROF is a mixture of Ir metal as well as crystallized IrO_X in the Rutile phase [16]. Rutile IrO_X has a primitive tetragonal lattice with a characteristic pair of peaks at 28 and 35° (ICDD PDF # 00–015-0870), and metallic Ir has a face-centered cubic lattice with a major peak at 41° (ICDD PDF # 00–006-0598) [40]. The predominantly high peak intensity at 35° indicates that the SIROF most likely takes preference for (101) texture, which is in line with the growth mechanism of platelet SIROF [39].

XPS analysis of SIROF is presented in Fig. 3b. The deconvolution of Ir 4f doublet and O 1 s are shown in Fig. 3(c-d), respectively, for further compositional analysis. The two primary peaks are assigned as Ir $4f_{7/2}$ at 61.8 eV which is mainly Ir^{4+} (characteristic of IrO_2), and Ir $4f_{5/2}$ at 64.8 eV corresponding to Ir^{4+} satellite peak. The O 1 s spectra consists of three peaks at 530.4 eV, 531.8 eV, and 533.4 eV, each corresponding to O–Ir–O interaction, hydroxide (O—H) bonds, and C–O/water bonds, respectively [10].

The atomic ratio between iridium and oxygen is calculated to be 1:2.15, which is slightly above the theoretical value 1:2 in stoichiometric IrOx. The physical origin of this oxygen enrichment can be attributed to adsorbed hydroxyl species or surface hydration arising from the interaction of the oxide surface with atmospheric water vapor. The overall results coincide with reported hydrous IrO2 films [10,41].

It is worth noting that there are uncertainties of 10% or above associated with XPS quantification, reflecting typical instrumental and sample-related factors such as surface sensitivity, peak fitting, and calibration [42,43]. To robustly confirm the elemental composition and stoichiometry, complementary elemental analysis techniques such as inductively coupled plasma (ICP) spectroscopy, or neutron scattering should ideally be employed alongside XPS measurements for comprehensive characterization.

One notable discrepancy with XRD results is that no distinct metallic Ir^0 peak is observed at the expected binding energy of 60.4 eV despite XRD evidence of metallic Ir in the bulk structure. This apparent discrepancy can be explained by two complementary mechanisms. Firstly, due to subsurface isolation where the metallic Ir may be located at depths beyond the XPS probing depth (3–5 nm vs. at least tens of nm for XRD probing) [14]. Therefore, it remains undetected due to electron attenuation. Secondly, due to rapid surface oxidation. Metallic Ir is thermodynamically unstable in atmospheric oxygen and readily surface-oxidizes during or immediately after deposition [44], forming a thin oxidized layer that masks the underlying metallic phase. This surface oxidation phenomenon is well-established for iridium and other noble metals and occurs on timescales of seconds to minutes under ambient conditions. Thus, the absence of Ir^0 in the XPS spectrum does not exclude the presence of metallic Ir in the bulk. The inclusion of iridium metal may strengthen the electrical conductivity of the material.

Bulk resistivity of SIROF was measured to be 580 ± 90 μΩcm (sheet

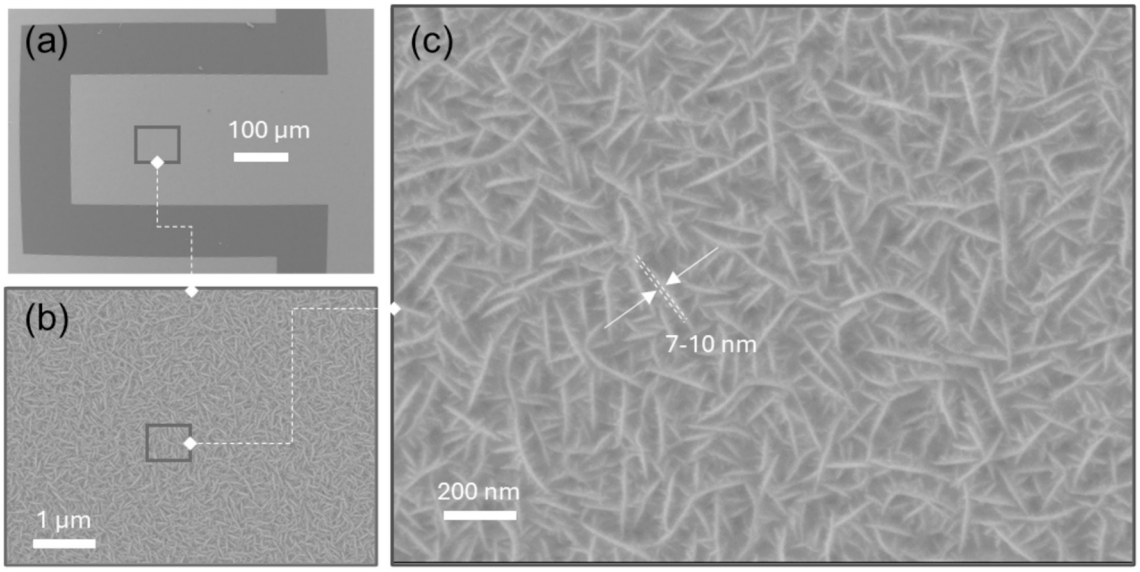

Fig. 2. (a-c) SEM images of platelet SIROF at different magnifications.

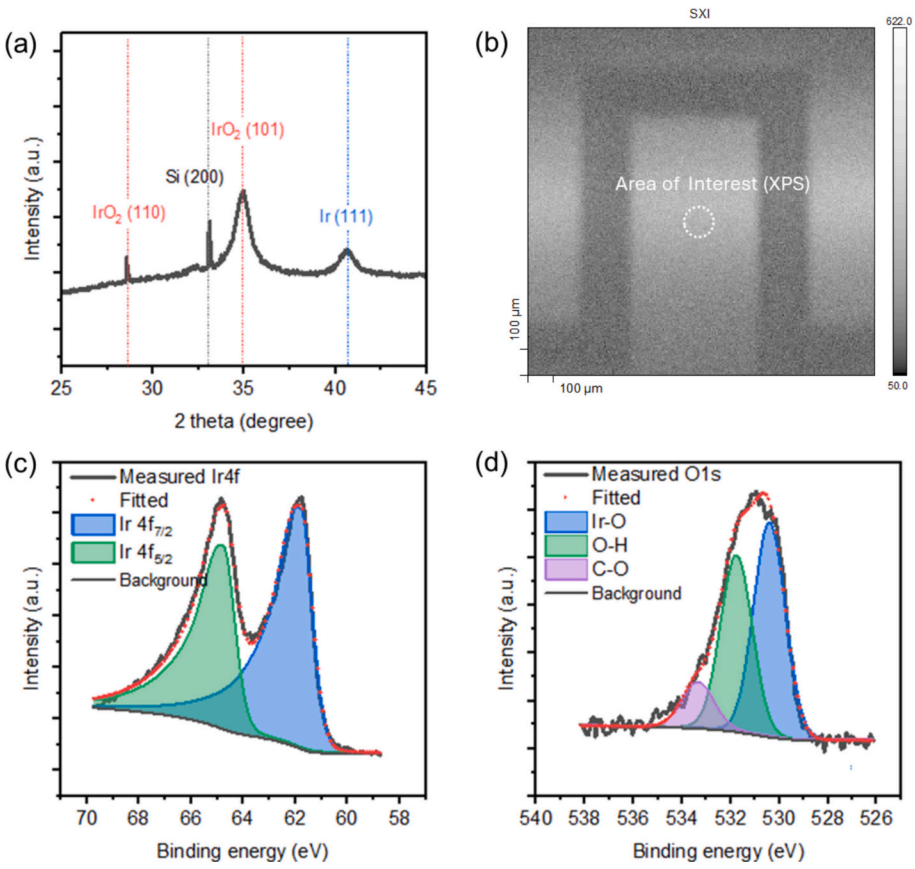

Fig. 3. (a) XRD pattern of SIROF on a silicon substrate, (b) Microscopic picture showing the area of interest for XPS characterization, (c) SIROF XPS spectra and fitting results of Ir4f, and (d) O1s.

resistance of 8.9 ± 0.5 Ω/sq. at nominal film thickness of 649 ± 64 nm), which is on par with a report of DC sputtered SIROF at 20 mTorr [16]. The resistivity is significantly lower than SIROFs sputtered at higher pressures and can be explained by the presence of Ir metallic crystallites embedded in the IrO_x film, which would decrease the resistivity of IrO_x films [10]. Moreover, sputtering at higher pressure results in higher porosity films, increasing the effective resistivity [16]. The bulk metallic Ir phase should exhibit substantially lower electrochemical activity compared to the predominant surface IrO_2 layer. The oxide shell should provide the majority of pseudocapacitive charge storage through reversible Ir^{3+}/Ir^{4+} redox reactions, while the metallic core serves the critical function of electronic conductivity, enabling efficient charge transport throughout the electrode architecture.

3.2. Evaluation of capacitive characteristics

Fig. 4(a–g) shows the CV curves at different scan rates ranging from 5 to 3000 mV s^{-1} for all the electrolytes with the exception of EMIM TFSI electrolyte, which ranges from 20 to 5000 mV s^{-1}. The selected scan rate range captures the full electrochemical behavior, including bulk diffusion and redox processes at low rates (to assess maximum capacitance) and high-rate performance to evaluate rate stability and power capability. In general, cyclic voltammograms (CVs) of all the devices exhibit nearly rectangular shapes indicating dominant capacitive charge storage containing EDL capacitance and pseudocapacitance.

In acidic electrolytes, the CV curves remained symmetric across the scan rate range. A pair of redox peaks was observed at ~0.3 V in H_2SO_4 (Fig. 4a) and ~ 0.1 V in H_3PO_4 (Fig. 4b). These redox peaks arise from the proton-coupled electron transfer reactions, where protons from the acidic electrolyte insert into and deinsert from the hydrated IrO_x structure to maintain charge neutrality. The positions of the peak are strongly influenced by the oxide's morphology, degree of hydration, and interactions with electrolyte anions. Phosphate species tend to interact more strongly with the oxide surface, often leading to slightly shifted redox features compared to sulfuric acid [45]. In the near-neutral pH electrolyte Na_2SO_4, the CV shape deviated from ideal capacitive behavior at low scan rates, with a rise in anodic current near 0.8 V (Fig. 4c). In PBS, semi-rectangular CV curves were observed with no significant current increase near 0.8 V (Fig. 4d). In the alkaline electrolyte NaOH, a current surge at low scan rates near 0.8 V was observed, similar to Na_2SO_4. At higher scan rates, the CV curves became rectangular, reflecting dominant capacitive behavior (Fig. 4e).

The gel electrolyte PVA/H_3PO_4 showed behavior similar to its aqueous counterpart, H_3PO_4, although the enclosed area (capacitance) at high scan rates was noticeably smaller. The redox pair remained visible at a similar voltage (Fig. 4f). For the ionic liquid EMIM TFSI, which supports higher operational voltages, the CV curves appeared semi-rectangular at higher scan rates. At very low scan rates, an exponential increase in current is observed above 1.5 V, which is attributed to the decomposition of residual moisture, as the MSCs were tested in open air with simple encapsulation. Although EmIm TFSI ionic liquid is reported to possess a stability window up to 4 V [46] under dry and inert conditions, the accessible voltage range in practical devices is strongly influenced by electrode potential and environmental factors. Therefore, the practical operating voltage in the present devices is limited to 2 V due to moisture-related side reactions, with reliable measurements obtained down to a minimum scan rate of 20 mV s^{-1} (Fig. 4g).

Fig. 4(h) presents the calculated capacitance values for SIROF in various electrolytes. The highest capacitance was observed at 5 mV s^{-1} in aqueous H_3PO_4, with an areal capacitance of 48.6 mF cm^{-2} and a volumetric capacitance of 810 F cm^{-3}. The second highest values were recorded for PVA/H_3PO_4 (43 mF cm^{-2} and 716.6 F cm^{-3}), followed by

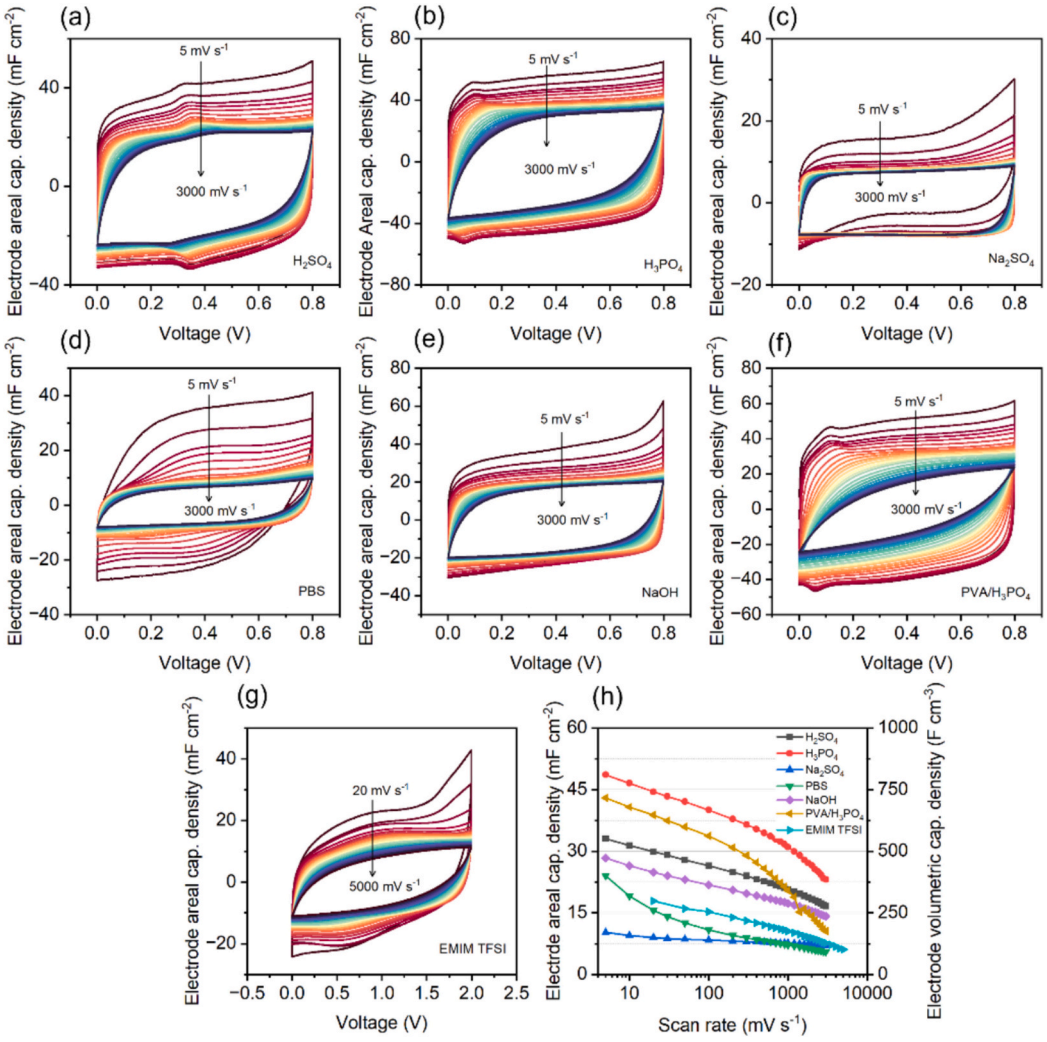

Fig. 4. CV curves of SIROF in (a) H_2SO_4, (b) H_3PO_4, (c) Na_2SO_4, (d) PBS, (e) NaOH, (f) PVA/H_3PO_4, and (g) EMIM TFSI, (h) Variation of capacitance with respect to scan rate (with measurement deviations maintained within 0.03–0.18% at all scan rates).

H_2SO_4. The lowest capacitance at 5 mV s^{-1} was found in Na_2SO_4 (10.2 mF cm^{-2} and 170 F cm^{-3}). However, Na_2SO_4 exhibited slower capacitance decay, retaining 68.68% of its capacitance at 3000 mV s^{-1}. In comparison, H_3PO_4, PVA/ H_3PO_4, and H_2SO_4 retained 47.5%, 24.5%, and 50.4% of their capacitance, respectively. In PBS, SIROF demonstrated a unique capacitance evolution with scan rate. At 5 mV s^{-1}, it achieved relatively high values of 24 mF cm^{-2} and 400 F cm^{-3}, but these dropped quickly with increasing scan rates to 100 mV s^{-1}. Beyond this, the values stabilized at levels similar to Na_2SO_4, with a retention of 22.8% at 3000 mV s^{-1}.

A high capacitance is typically associated with fast interfacial kinetics, characteristics of EDL capacitance and pseudocapacitance, with limited participation of irreversible reactions. The difference in the dependence of capacitance on scan rate across devices with different electrolytes highlights that the underlying charge storage processes are strongly influenced by the electrolyte environment. A rigorous quantitative analysis would be required to clearly distinguish these underlying processes. However, such an analysis typically necessitates a three-electrode configuration, which is beyond the scope of the present study and will be addressed in future work. In this work, we instead employ a semi-quantitative assessment based on the two-electrode device CV curves (see Supporting Information, section "Supplementary analysis: Quantification of charge storage mechanisms") as qualitative indicators of relative trends.

As can be seen from Fig. S5 and Table S3 that the device using H_3PO_4 exhibits the highest capacitive contribution, followed by H_2SO_4 and PVA/H_3PO_4. In contrast, although the MSC with PBS displays relatively high capacitance, a significant portion (84%) of it is attributed to diffusion-controlled capacitance, with the remaining 16% originating from capacitive charge storage. This reduced capacitive charge storage in PBS, compared to strong acids (H_3PO_4, H_2SO_4), a strong base (NaOH), or neutral salt (Na_2SO_4), is likely due to several interrelated factors. These include the lower ionic strength of PBS (typically the ionic concentration is in the millimolar range versus at least 1 M in other systems), the presence of large, multivalent phosphate-based ions ($H_2PO_4^-$, HPO_4^{2-}), and the buffering nature of the solution. Together, these characteristics reduce ion mobility, limit efficient ionic packing, and impair electrostatic screening at the interface, ultimately lowering double-layer capacitance [47,48].

Similarly, the pseudocapacitive behavior of IrO_x is highly sensitive to electrolyte composition, primarily influenced by pH and the nature of ionic species. In strongly acidic electrolytes such as H_2SO_4 and H_3PO_4, the high proton concentration facilitates rapid and reversible Ir^{3+}/Ir^{4+} redox transitions, yielding high capacitance values due to efficient pseudocapacitive charge storage [49]. In contrast, PBS offers a buffered environment with limited proton availability that leads to slower pseudocapacitive kinetics. Consequently, diffusion-controlled processes become dominant.

Similarly, in the case of the ionic liquid EMIM TFSI, the viscous nature and associated ion crowding hinder fast ion transport, resulting in slow kinetics and a diffusion-limited charge storage mechanism. Neutral electrolytes such as Na_2SO_4 are expected to exhibit minimal pseudocapacitive behavior due to the lack of protons necessary for redox activity, resulting in relatively low capacitance. Alkaline electrolytes like NaOH also show suppressed proton-coupled redox activity due to low H^+ concentration. In such environments, pseudocapacitance may arises from higher oxidation state transitions (e.g., Ir^{4+}/Ir^{5+}) [50], rather than the more reversible surface-confined proton insertion/extraction processes that happens in acidic media. However, these transitions are less reversible [51] and may compromise long-term stability through dissolution of IrO_x.

Furthermore, device stability can be challenged when operating voltages approach the electrochemical window limits of the systems. Under such conditions, minor Faradaic processes such as water oxidation can occur, leading to oxygen evolution reactions in aqueous systems [52] as seen in Fig. 4 (c) and 4 (e). In EMIM TFSI, parasitic Faradaic reactions associated with ionic liquid decomposition or residual water oxidation can also emerge at high anodic potentials [53] as seen in Fig. 4 (g). These electrolyte-dependent variations in SIROF performance underscore the critical role of interfacial redox processes and highlight the need for further mechanistic investigation, ideally in a three-electrode configuration to decouple electrode-specific behaviors.

3.3. Device-level performance

The diverse applications of MSCs require tailored compatibility of electrode or electrolyte depending on whether the primary requirement is high capacitance, power density or energy density, or operation under different environments. In this section we discuss the compatibility of the SIROF electrode with different electrolytes in terms of device level performance with GCD analysis as it is of greater relevance to practical application scenarios. For instance, in practical devices, MSCs are typically operated under constant current conditions during both charging and discharging processes. Therefore, GCD directly reflects how a device performs when subjected to realistic operational loads and enables the estimation of practical parameters such as, coulombic efficiency, energy and power density, and cyclic stability under conditions analogous to actual device operation.

a) Assessment of device behavior in biocompatible PBS electrolyte

Owing to its excellent biocompatibility, SIROF has been extensively utilized in neural electrical stimulation applications and is gaining attention as a candidate electrode material for implantable energy storage systems [10]. In such bioelectronic applications, PBS is commonly employed as the electrolyte due to its biocompatibility, and physiological relevance. While in vivo conditions typically require temperature control at 37 °C to replicate physiological conditions, the present study was conducted at RT (21 °C) to enable direct performance comparison with conventional electrolytes used in microscale energy storage devices.

Fig. 5 (a-c) presents GCD curves at current densities ranging from 10 to 1000 μA cm^{-2}, with the corresponding areal capacitance values shown in Fig. 5(d). As the current density increases, both the charging and discharging times decrease, indicating faster charging and discharging at higher current densities. Consequently, the capacitance also decreases, retaining nearly 25% at 1000 μA cm^{-2} compared to the value at 10 μA cm^{-2}. Self-discharge behavior is evaluated and presented in Fig. 5(e). After charging to 0.8 V and holding the voltage for 30 min, the device is left in open-circuit condition, and the voltage decay is monitored. After 1 h of self-discharge, some 67% (0.54 V) of the initial voltage is retained, which is consistent with the intrinsic behavior of supercapacitors, where self-discharge arises from thermodynamic driving forces. The selection of self-discharge duration of 1 h is chosen as to provide a practical basis for comparing charge retention while remaining relevant to intended operation over short duty cycles of on-chip microsystems. While unavoidable, the rate of self-discharge can be kinetically suppressed through strategic modifications to structural

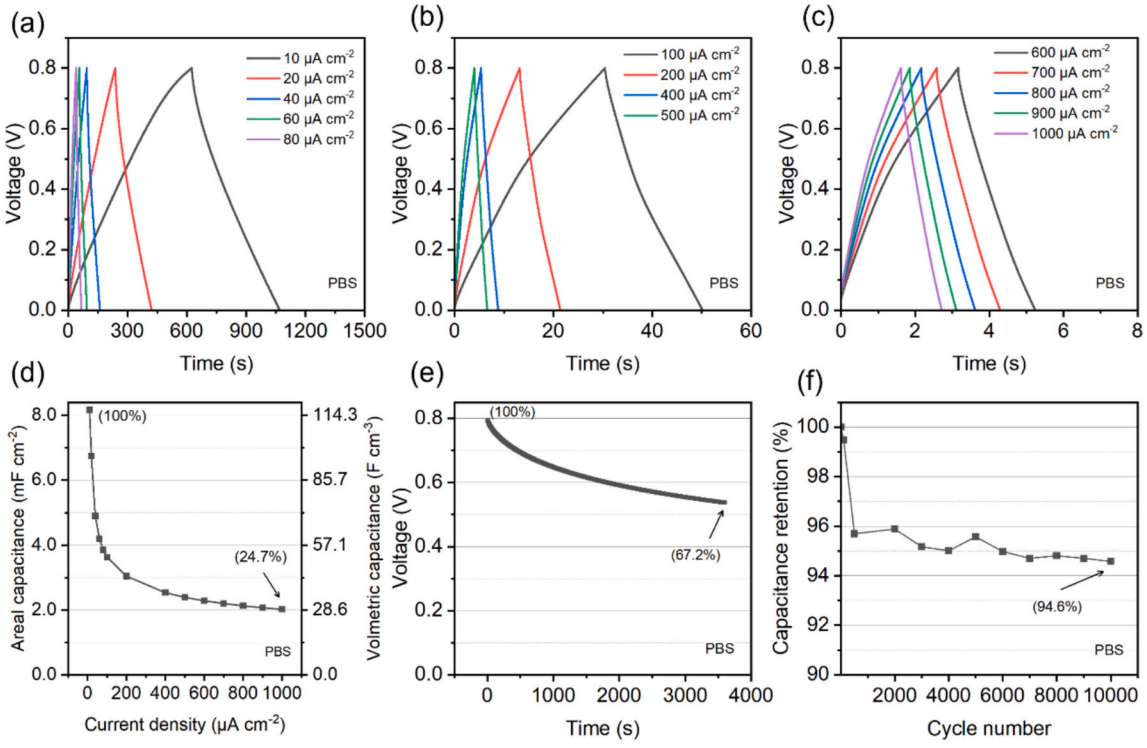

Fig. 5. Electrochemical performance of SIROF in PBS: (a-c) GCD curves at various current densities, (d) Variation of capacitance with respect to scan rate, (e) Self-discharge within 1 h, (f) Cycling stability with a current density of 500 μA cm^{-2}.

components such as electrodes, electrolytes, separators, and current collectors [54].

Finally, cycling stability is assessed by performing GCD cycles at a current density of 500 μA cm^{-2} for 10,000 cycles. At the end of cycling, 5.4% of the initial capacitance is lost, indicating excellent stability. Overall, the SIROF-PBS MSC demonstrates high efficiency and stability, with rapid charging/discharging capabilities and minimal capacitance loss over time (approximately 15 h) and usage cycles.

b) Performance evaluation under elevated temperature conditions

Ionic liquid electrolytes are well-suited for MSCs operating at elevated temperatures due to their superior thermal tolerance and wide electrochemical stability window. Their ability to sustain higher operating voltages enhances energy and power densities, while their stability across broad temperature ranges supports operation in harsh environments, unlike traditional aqueous or organic electrolytes, which may degrade. Here, we demonstrate that the SIROF-based MSC can operate with the EMIM TFSI ionic liquid, offering enhanced operating voltage and potential for high-temperature applications.

The GCD curves at RT and at 60 °C are shown in Fig. 6 (a-c) and 6 (d-f), respectively, within a voltage window of 0 to 2 V. At the lowest current density of 100 μA cm^{-2}, the charging curve at RT begins to bend at 1.5 V, suggesting the onset of side reactions, consistent with the observations in the CV characterizations (Fig. 4g). At 60 °C, the charging curve at 100 μA cm^{-2} is more significantly distorted, indicating more pronounced side reactions as the electrode is held at high potentials for longer times allowing slow parasitic process such as, thermal activation

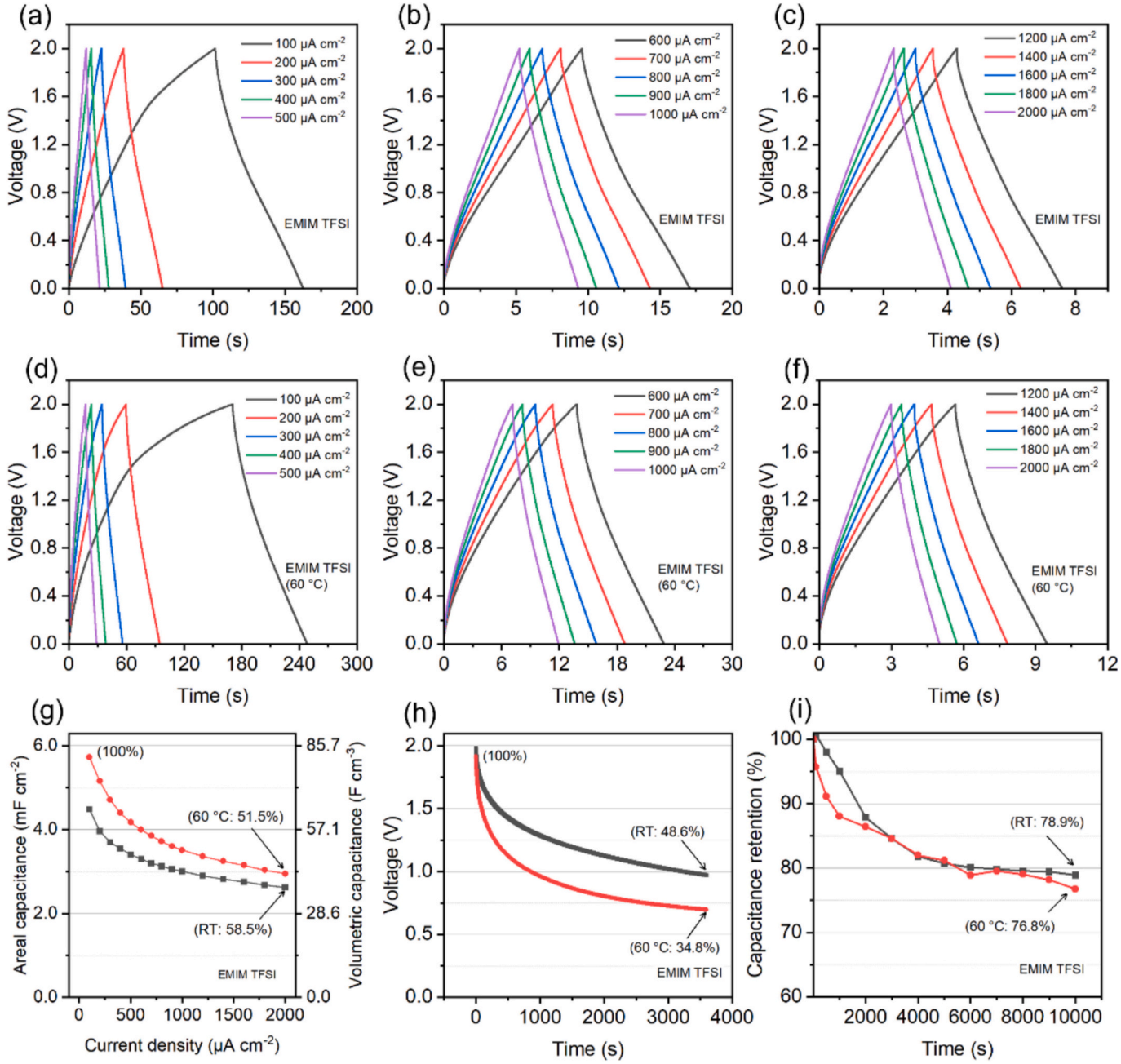

Fig. 6. Electrochemical performance of SIROF in EMIM TFSI: (a-c) GCD curves at various current densities at room temperature (RT), (d-f) GCD curves at various current densities at elevated temperature (60 °C), (g) Variation of capacitance with respect to scan rate, (h) Self-discharge within 1 h, (i) Cycling stability at 1000 μA cm^{-2} at RT and 2000 μA cm^{-2} at 60 °C.

of Imidazolium cation or partial decomposition of $TFSI^-$ anion [55] to occur specially in the presence of moisture. As the current density increases, both the charging and discharging curves become more linear and symmetric, suggesting that the side reactions are likely diffusion limited.

As shown in Fig. 6g, the areal capacitance at elevated temperatures surpasses that measured at room temperature (RT). This enhancement is primarily attributed to the reduction in equivalent series resistance (ESR), which decreases from 22.9 Ω cm^2 at RT to 12.97 Ω cm^2 at 60 °C, as evidenced by the Nyquist plot in the EIS spectrum (Fig. S7). The ESR typically arises from both external circuit elements and the intrinsic resistance of the electrolyte, with the latter contributing most significantly. The ESR values for all the electrolytes can be found in the supporting information Table S6. The observed decrease in ESR with increasing temperature can be correlated with improved ionic conductivity of the electrolyte. Specifically, the ionic conductivity of EMIM TFSI increases from 3.2 mS cm^{-1} at RT to 8.0 mS cm^{-1} at 60 °C, facilitating faster ion transport and more efficient charge storage [56]. However, the higher temperature also promotes greater self-discharge, leading to lower voltage retention at 60 °C (35%) compared to RT (49%) under the same test conditions, as shown in Fig. 6 (h). Fig. 6 (i) presents the cycling stability, where both RT and 60 °C show similar capacitance retention after 10,000 cycles, with values of 79% and 77%, respectively. Because ionic liquid electrolytes are sensitive to moisture levels, and the SIROF-EMIM TFSI system is not hermetically sealed in this study, we believe that a more controlled testing environment and improved device encapsulation can reduce side reactions related to water decomposition, resulting in better capacitance retention during long-term stability tests.

c) Scalable MSC architectures for voltage and capacitance modulation

Liquid electrolytes often face issues such as leakage, volatility, and limited mechanical stability, which can compromise device scalability, safety, and longevity. To address these challenges, gel electrolytes have emerged as a competitive alternative. They retain the relatively high ionic conductivity of liquid electrolytes while offering enhanced safety and flexibility due to their semi-solid nature. Gel electrolytes minimize the leakage risks and provide better structural integrity, making them ideal for miniaturized, flexible, and wearable electronics [36,37].

Here, we demonstrate the operation of the SIROF-based MSC with a PVA/H_3PO_4 gel electrolyte. Additionally, we evaluate MSCs connected in series and parallel to fully assess their performance in practical applications. Series connections allow MSCs to achieve higher voltage outputs, which are essential for devices requiring increased operating voltages, while parallel connections enhance the overall capacitance and energy storage capacity, enabling longer operational times. Understanding how these configurations impact parameters such as charging and discharging behavior and cycle life is crucial for optimizing MSC design and integration in real-world systems.

Fig. 7 (a-c) presents the GCD curves for a single PVA/H_3PO_4 device (denoted as 1×), two or three PVA/H_3PO_4 devices connected in series (denoted as 2S and 3S), and two PVA/H_3PO_4 devices connected in parallel (denoted as 2P). For comparative analysis, data from a single device employing aqueous H_3PO_4 electrolyte were also included. As anticipated, the device incorporating the gel electrolyte (PVA/H_3PO_4) exhibited a decrease in areal capacitance across the full range of current densities, particularly at higher current loads, as shown in Fig. 7(d). The incorporation of PVA into the electrolyte matrix increases the interfacial resistance, as reflected by a significant rise in the ESR from 3.70 Ω cm^2 for the liquid electrolyte to 13.5 Ω cm^2 for the gel electrolyte, as illustrated by the Nyquist plot in the EIS spectrum (Fig. S8). Similarly, the ionic conductivity also decreases with the addition of the PVA in the electrolyte (Fig. S9). Additionally, the dielectric relaxation time constant (τ_0), derived from the frequency at which the phase angle reaches to −45°, also increases in the gel electrolyte, 160 ms to 500 ms, indicating slower charge transport kinetics. Nevertheless, at low current densities or at the lowest frequency, the extended time available for ion migration

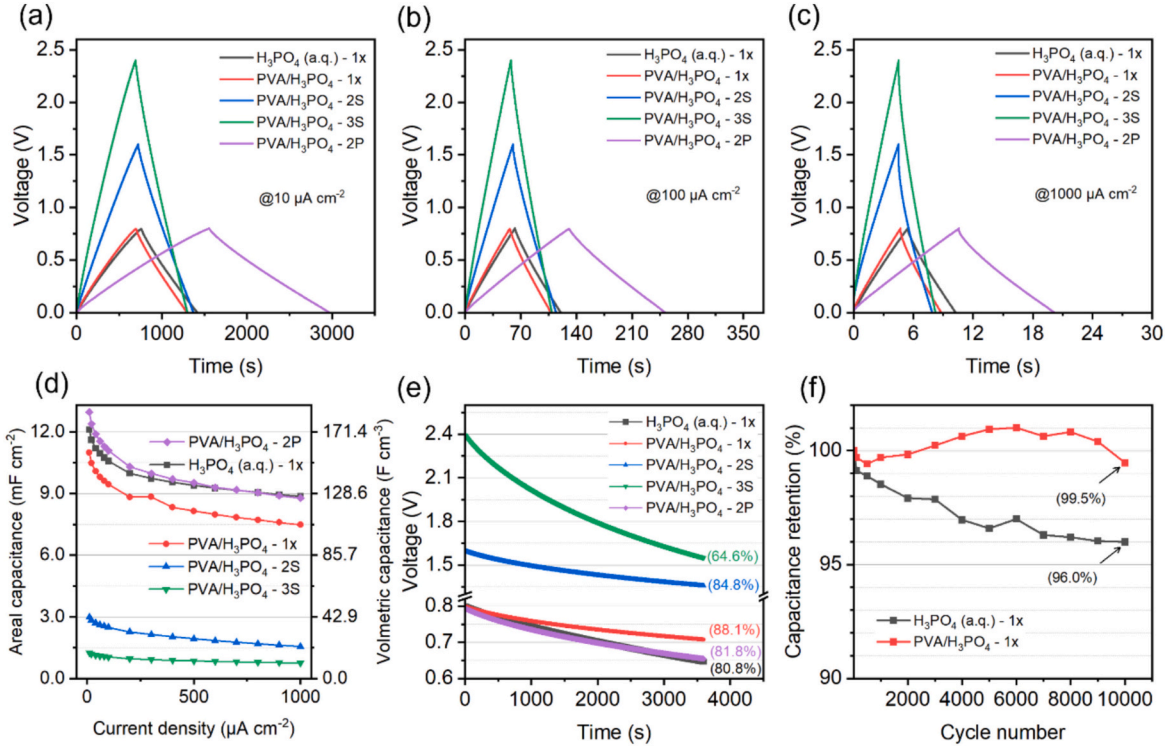

Fig. 7. Electrochemical performance of SIROF in PVA/H_3PO_4 and H_3PO_4 electrolytes and different connections: 1× - single device, 2S – 2 devices connected in series, 3S - 3 devices connected in series, 2P – 2 devices connected in parallel: (a-c) GCD curves at various current densities, (d) Variation of capacitance with respect to current density, (e) Self-discharge within 1 h, (f) Cycling stability at 1000 μA cm^{-2}.

and charge transfer partially offsets the slower kinetics, resulting in relatively smaller differences in capacitance between the gel and liquid counterparts (Fig. S7).

When the devices are connected in series as expected, the 2S and 3S devices can operate at higher voltages of up to 1.6 V and 2.4 V, respectively, although their charging and discharging curves are no longer linear. For the 2P devices, the charging and discharging times are approximately doubled compared to the 1× or aqueous H_3PO_4 device. The normalized capacitance densities are shown in Fig. 7(d). Aqueous H_3PO_4, PVA/H_3PO_4 (1×), and PVA/H_3PO_4 (2×) form the first group, with a maximum capacitance density of over 10 mF cm^{-2}. The areal capacitance for the 2S and 3S devices is roughly 1/4 and 1/9 of that for the 1× device. The deviation from theoretical capacitance values can be attributed to subtle differences between individual devices, such as variations in film thickness and electrode footprint area, which could result in imbalanced charging. This imbalance may overcharge one component, leading to higher capacitance. These differences could also explain the varying voltage retention during self-discharge tests.

Ideally, all PVA/H_3PO_4 devices, whether single, in series, or parallel, should exhibit the same self-discharge behavior (voltage retention) when operated within their respective voltage windows. However, the slowest self-discharge is observed for the 1× device (88.1%), with series and parallel connections showing worse voltage retention, likely due to overcharging caused by an imbalance among the connected devices. The PVA/H_3PO_4 1× device outperforms the liquid H_3PO_4 1× device, which loses an additional 50 mV within the same self-discharge period. While self-discharge cannot be completely eliminated due to its thermodynamic nature, its rate can be mitigated by slowing down the kinetics of the related processes [57]. The use of gel electrolytes demonstrates the potential for achieving slower self-discharge and lower leakage by restricting the kinetics within the electrolyte.

Finally, the cycling stability of PVA/H_3PO_4 is compared with that of aqueous H_3PO_4 in Fig. 7(f). Both PVA/H_3PO_4 and liquid H_3PO_4 show excellent cycling stability, with capacitance retention of 99.5% and 96.0%, respectively, after 10,000 cycles. The GCD curves at different cycle numbers are shown in Fig. S10.

d) Solar-powered charging and energy delivery of SIROF-based MSCs

To assess the practical applicability of SIROF-based MSCs in real-world energy harvesting scenarios, we investigated their performance under solar charging using commercially available photovoltaic cells with varying output voltages. A flexible PowerFilm solar cell (Model: INP1.2-12 × 34), with an open-circuit voltage of approximately 1 V, was employed to charge a single MSC device without any external bias. In-situ chronopotentiometric measurements were carried out to evaluate the charging–discharging behavior under solar illumination as schematically illustrated in the equivalent circuit diagram in Fig. 8a. The single MSC with the PVA/H_3PO_4 electrolyte was charged to 0.8 V and discharged with current densities ranging from 10 to 500 μA cm^{-2} as shown in Fig. 8 (b–c), highlighting its potential for integration in self-sustaining, low-power systems.

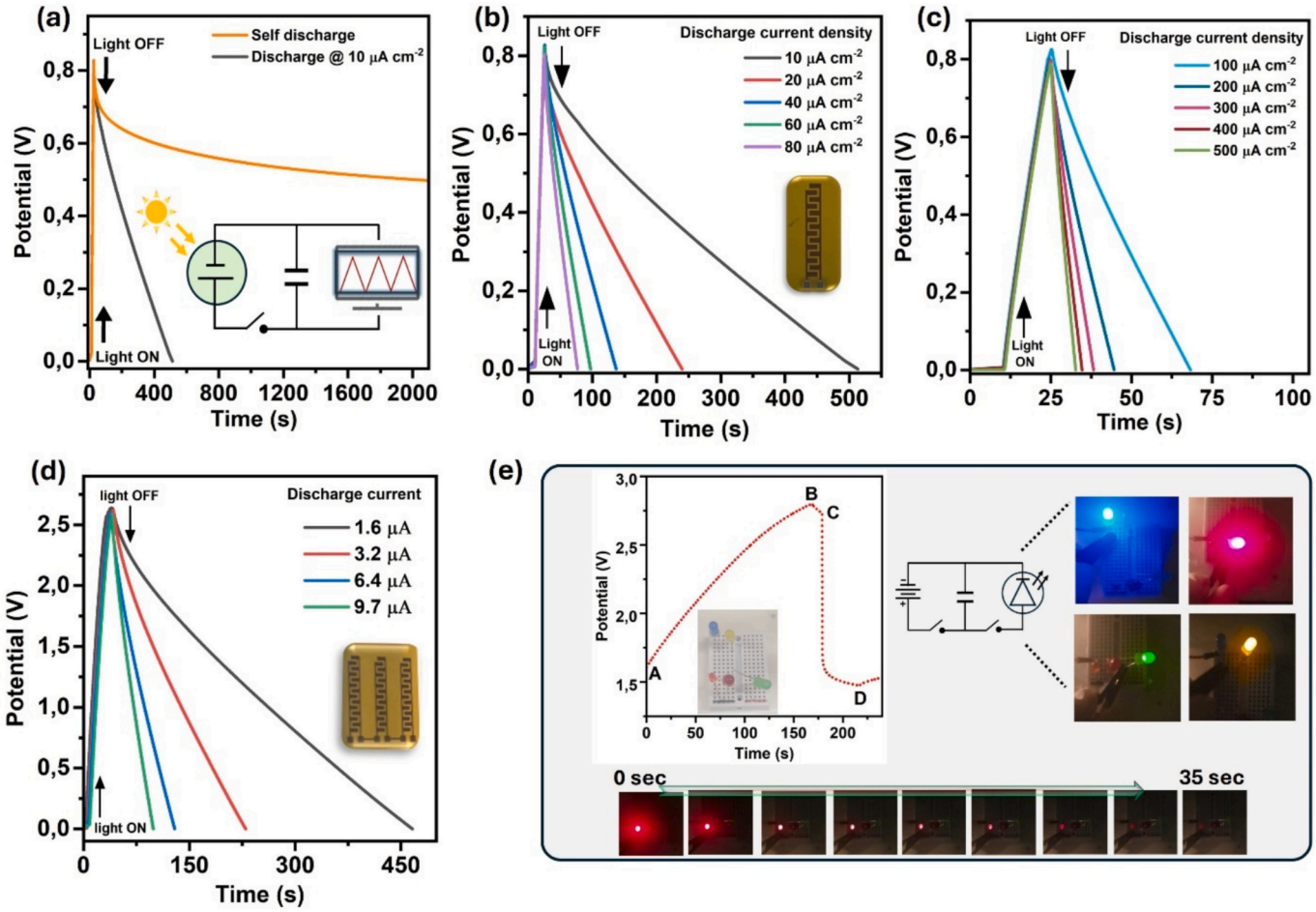

Fig. 8. Solar charging of a single MSC using Si solar cell by PowerFilm with, (a) chrono potentiometric profiles of the same device with and without applied discharge current and an inset of equivalent circuit for solar charging of MCS and data acquisition, (b) discharge rate at relatively lower current densities with an inset of single MSC image, (c) discharge rate at relatively higher current densities, (d) Solar charging of 3-MSCs in series using a Si solar cell by Panasonic with an inset image of 3-MSCs in series, (e) set of experiments with 3-MSCs devices in series charged to 2.8 V and used to light various LEDs.

To further demonstrate the scalability of the MSC architecture, a module comprising three MSCs connected in series (3S) was charged using a higher-voltage Panasonic solar cell (Model: AM-1456CA-DGK-E). Under illumination, the series-connected MSC module rapidly achieved a voltage of 2.6 V. It was subsequently discharged under dark conditions at various current levels (Fig. 8d), demonstrating its ability to support higher voltage operations, which are relevant to practical microelectronic applications.

The energy storage capabilities of the SIROF-based MSCs were further demonstrated by powering light-emitting diodes (LEDs) of different colors and threshold voltages, as shown in Fig. 8e. The red LED, requiring a forward voltage of 1.4 V, was illuminated for several seconds, showcasing the MSC's capacity for short-term autonomous power delivery. The corresponding in-situ chronopotentiometric profile is presented in Fig. 8e, outlining three distinct operational phases. The first phase (A to B) represents the solar charging phase at a constant current of 3.2 μA, where the device voltage gradually increases to 2.8 V. The second phase (B to C) corresponds to the intrinsic self-discharge phase, where a gradual voltage drop occurs due to internal leakage, and energy dissipation occurs within the system. The third phase (C to D) denotes the LED lighting phase, during which the stored energy is discharged through the connected LED. The voltage decreases as the MSC delivers power to the LED, with the duration and intensity of illumination depending on the MSC's capacity and the LED's threshold voltage.

These results show the capability of SIROF-based MSCs to interface directly with commercial solar cells and efficiently store and deliver energy in a voltage-dependent manner, demonstrating promise for integration into self-powered microsystems and intermittent energy harvesting platforms, as shown in Fig. S1.

3.4. Performance overview

Despite its relatively high cost compared to other transition-metal oxides, IrO_x remains an attractive material for targeted energy storage applications due to its unique combination of physicochemical and electrochemical properties. They can be synthesized in various nanostructured forms, including amorphous nanopowders, nanosheets, nanorods, nanotubes, nanowires, and nanoporous films [9]. These morphological variations substantially influence the electrochemical behavior of IrO_x-based supercapacitors, especially under different device architectures and electrolyte environments. As a result, direct performance comparison across systems is often challenging.

Liu et al. [58] investigated the effect of post-deposition annealing on RF-sputtered IrO_2 thin films deposited on stainless steel substrates, with annealing temperatures ranging from RT to 300 °C. Electrochemical measurements were performed in 1 M $LiNO_3$ within a potential window of 0 to 1 V. A progressive decline in specific capacitance was observed, decreasing from 293 to 226 F g^{-1} with increasing annealing temperature. This reduction in performance was attributed to a transition from an initially amorphous phase to a more crystalline structure, leading to a decreased electrochemically active surface area and diminished pseudocapacitive behavior. Additionally, amorphous hollow IrO_2 nanofibers (45 nm diameter) were synthesized via single-nozzle electrospinning [7]. The electrode material exhibited capacitive behavior in both anodic and cathodic directions over a 1 V potential window (vs. SCE) in 1 M Na_2SO_4. When assembled into a symmetric solid-state device using a $LiClO_4$–PVA gel electrolyte, the nanofibers delivered a specific capacitance of 102 F g^{-1} (15 mF cm^{-2}) at 1 mA cm^{-2}, retaining 60% of the capacitance at 3 mA cm^{-2}.

Other studies have explored IrO_x-based composite electrodes, such as porous ZnO coated with Ir/IrO_2 via physical vapor deposition followed by annealing. These electrodes exhibited an areal capacitance of 5.25 mF cm^{-2} in 0.8 V aqueous LiCl, with 90% retention after 10,000 cycles [59]. Composite structures of IrO_2 nanotubes with multiwalled carbon nanotubes (MWCNTs), prepared by chemical vapor deposition, significantly enhanced the capacitance to 69 F g^{-1} from 15 F g^{-1} for pristine MWCNTs, highlighting the contribution of IrO_2's pseudocapacitive properties in 0.1 M KOH electrolyte [24]. Similarly, a MnO_2/IrO_2 composite (70:30 mol%) prepared by thermal decomposition at 450–550 °C exhibited a specific capacitance of 557 F g^{-1} in 0.5 M H_2SO_4 over a potential range of 0.4–1.4 V vs. RHE, due to a synergistic combination of electric double-layer and surface Faradaic charge storage mechanisms [60].

Similarly, the electrochemical performance of SIROF-based MSCs in this study exhibits substantial variation depending on the electrolyte used. Strong acidic electrolytes such as H_2SO_4, H_3PO_4, and PVA/H_3PO_4 gel demonstrated significantly higher capacitance values compared to neutral (Na_2SO_4, PBS) and alkaline (NaOH) systems. This enhancement is attributed to the abundance of protons in acidic media, which facilitates fast surface-confined redox reactions. In contrast, PBS, characterized by limited proton availability and low ionic concentration (10 mM), exhibits lower capacitance governed predominantly by diffusion-controlled charge storage.

Nevertheless, neutral electrolytes offer a broader electrochemical stability window, allowing the operating voltage to be extended up to 1.6 V by leveraging the overpotentials of the hydrogen and oxygen evolution reactions (Fig. S11). This increase in voltage can directly contribute to a twofold enhancement in both energy and power density illustrated in the Ragone plot (Fig. 9). Among the tested electrolytes, EMIM TFSI ionic liquid exhibited the highest energy density, especially at elevated temperatures, benefiting from a wide electrochemical window of up to 2 V.

The observed capacitive performance is strongly influenced by the intrinsic platelet-like morphology of the SIROF films, which provides a high electrochemically active surface area [8] and metallic-like conductivity [9], promoting rapid charge transfer and efficient ion diffusion. Furthermore, the use of identical electrode materials across all systems enabled a clearer understanding of the electrolyte–electrode interfacial dynamics. Ultimately, the choice of electrolyte should be guided by the targeted application, whether emphasizing high power, energy density, operational voltage, or long-term cycling stability. A brief comparison of the performance metrics of the SIROF MSC can be found in the supporting information (Table S7).

4. Conclusions

This study demonstrates the suitability of SIROF electrodes with platelet morphology as a promising electrode material for MSC applications. The unique morphology of SIROF provides a high electrochemical surface area and facilitates efficient electron and ion transport, contributing to enhanced capacitive performance across a range of electrolytes, highlighting their versatility in various electrolytes. Among aqueous systems, acidic electrolytes, particularly H_3PO_4 and PVA/H_3PO_4 gel electrolyte, exhibited the highest areal capacitance and energy density, with the gel electrolyte offering additional benefits such as improved mechanical safety and suppressed self-discharge, making it particularly attractive for flexible and wearable applications.

The incorporation of EMIM TFSI ionic liquid extended the operating voltage window up to 2 V, thereby enhancing both energy and power densities, demonstrating excellent potential for high-energy applications in extreme environments, although its performance was impacted by moisture sensitivity. Practical applications were validated through series and parallel configurations of SIROF-based MSCs, as well as successful charging via solar cells, underscoring their versatility for energy harvesting and storage in modern electronics.

Future research should focus on exploring the interactions between SIROF electrodes and electrolytes, particularly in three electrode systems, to further refine the understanding of the capacitive and Faradaic processes. Techniques such as electrochemical quartz crystal microbalance (EQCM) or spectroelectrochemistry could provide valuable insight in that direction. Improved encapsulation techniques will also be necessary to mitigate moisture-related challenges, especially for ionic

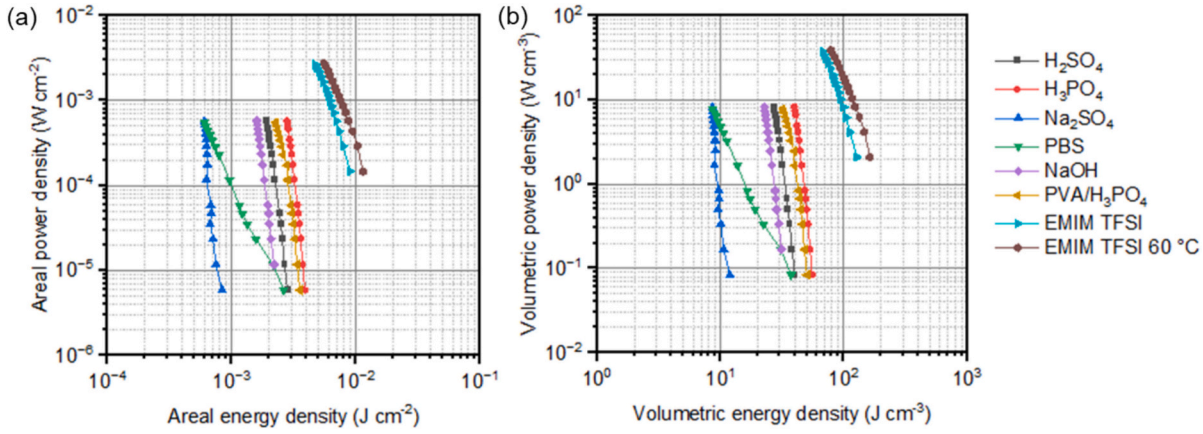

Fig. 9. Ragone plots of SIROF MSCs with various electrolytes.

liquid-based devices. Overall, SIROFs have been shown to be scalable, efficient, and versatile electrode materials that can significantly advance the development of next-generation miniaturized energy storage technologies.

CRediT authorship contribution statement

Qi Li: Writing – original draft, Visualization, Resources, Methodology, Investigation, Formal analysis, Data curation, Conceptualization. **Lukas Matter:** Writing – review & editing, Validation, Resources, Methodology, Investigation, Formal analysis, Conceptualization. **Muhammad Hassan:** Writing – review & editing, Visualization, Validation, Methodology, Investigation, Formal analysis. **R.K. Azega:** Writing – review & editing, Methodology, Investigation, Formal analysis. **Hanna Karlsson-Fernberg:** Writing – review & editing, Resources, Investigation. **Björn Wickman:** Writing – review & editing, Resources. **Johan Liu:** Writing – review & editing, Resources, Funding acquisition. **Maria Asplund:** Writing – review & editing, Resources, Funding acquisition. **Per Lundgren:** Writing – review & editing, Supervision, Project administration, Funding acquisition, Conceptualization. **Mazharul Haque:** Writing – review & editing, Visualization, Validation, Supervision, Resources, Project administration, Methodology, Investigation, Formal analysis, Data curation, Conceptualization.

Declaration of competing interest

The authors declare that they have no known competing financial interests or personal relationships that could have appeared to influence the work reported in this paper.

Acknowledgements

The authors gratefully acknowledge the European Union‘s Horizon 2020 research and innovation program under Grant Agreement No. 101006963 (GreEnergy). Further support was provided by the Chalmers Gender Initiative for Excellence (GENIE) and the European Union's Horizon 2020 research and innovation program under grant agreement No. 101099366 (BioFINE). We also acknowledge the support provided by the 2D-tech Vinnova competence center.

Appendix A. Supplementary data

Supplementary data to this article can be found online at https://doi.org/10.1016/j.est.2026.121720.

Data availability

Data will be made available on request.

References

[1] Y. Xu, S. Yu, H.M. Johnson, Y. Wu, X. Liu, B. Fang, Y. Zhang, Recent progress in electrode materials for micro-supercapacitors, Iscience 27 (2) (2024).
[2] W. Wang, L. Xu, L. Zhang, A. Zhang, J. Zhang, Self-powered integrated sensing system with in-plane micro-Supercapacitors for wearable electronics, Small 19 (29) (2023) 2207723.
[3] A. Smith, Q. Li, A. Vyas, M.M. Haque, K. Wang, A. Velasco, X. Zhang, S. Thurakkal, A. Quellmalz, F. Niklaus, Carbon-based electrode materials for microsupercapacitors in self-powering sensor networks: present and future development, Sensors 19 (19) (2019) 4231.
[4] S. Deka, Nanostructured mixed transition metal oxide spinels for supercapacitor applications, Dalton Trans. 52 (4) (2023) 839–856.
[5] K. Wang, H. Wu, Y. Meng, Z. Wei, Conducting polymer nanowire arrays for high performance supercapacitors, Small 10 (1) (2014) 14–31.
[6] R. Liang, Y. Du, P. Xiao, J. Cheng, S. Yuan, Y. Chen, J. Yuan, J. Chen, Transition metal oxide electrode materials for supercapacitors: a review of recent developments, Nanomaterials 11 (5) (2021) 1248.
[7] S. Beknalkar, A. Teli, N. Harale, D. Patil, S. Pawar, J. Shin, P. Patil, Fabrication of high energy density supercapacitor device based on hollow iridium oxide nanofibers by single nozzle electrospinning, Appl. Surf. Sci. 546 (2021) 149102.
[8] L. Matter, O.S. Abdullaeva, S. Shaner, J. Leal, M. Asplund, Bioelectronic direct current stimulation at the transition between reversible and irreversible charge transfer, Adv. Sci. 11 (27) (2024) 2306244.
[9] F. Scarpelli, N. Godbert, A. Crispini, I. Aiello, Nanostructured iridium oxide: state of the art, Inorganics 10 (8) (2022) 115.
[10] N. Geramifard, B. Chakraborty, B. Dousti, G.S. Lee, J. Maeng, High-energy-density sputtered iridium oxide micro-supercapacitors operating in physiological electrolytes, J. Electrochem. Soc. 169 (5) (2022) 050508.
[11] B. Harland, L. Matter, S. Lopez, B. Fackelmeier, B. Hazelgrove, S. Meissner, S. O'Carroll, B. Raos, M. Asplund, D. Svirskis, Daily electric field treatment improves functional outcomes after thoracic contusion spinal cord injury in rats, Nat. Commun. 16 (1) (2025) 1–16.
[12] S.F. Cogan, Neural stimulation and recording electrodes, Annu. Rev. Biomed. Eng. 10 (1) (2008) 275–309.
[13] M. Rivas, R.Q. Rudy, B. Sanchez, M.B. Graziano, G.R. Fox, P. Sunal, L. Nataraj, E. Sandoz-Rosado, A.C. Leff, B.D. Huey, Iridium oxide top electrodes for piezo-and pyroelectric performance enhancements in lead zirconate titanate thin-film devices, J. Mater. Sci. 55 (2020) 10351–10363.
[14] C. Roiron, C. Wang, I.V. Zenyuk, P. Atanassov, Oxygen 1s x-ray photoelectron spectra of iridium oxides as a descriptor of the amorphous–rutile character of the surface, The Journal of Physical Chemistry Letters 15 (45) (2024) 11217–11223.
[15] N. Page, J. Lucchi, J. Buchan, A. Fones, H. Hamilton, T. Scabarozi, L. Yu, S. Amini, J. Hettinger, The effect of deposition parameters on microstructure and electrochemical performance of reactively sputtered iridium oxide coatings, Mater. Today Commun. 29 (2021) 102967.
[16] S. Negi, R. Bhandari, L. Rieth, F. Solzbacher, Effect of sputtering pressure on pulsed-DC sputtered iridium oxide films, Sens. Actuators B 137 (1) (2009) 370–378.
[17] Q. Li, A.D. Smith, A. Vyas, F. Cornaglia, A. Anderson, M. Haque, P. Lundgren, P. Enoksson, Finger number and device performance: a case study of reduced graphene oxide microsupercapacitors, Phys. Status Solidi B 258 (2) (2021) 2000354.
[18] T. De Silva, C. Damery, R. Alkhaldi, R. Karunanithy, D.H. Gallaba, P.D. Patil, M. Wasala, P. Sivakumar, A. Migone, S. Talapatra, Carbon nanotube based robust

and flexible solid-state supercapacitor, ACS Appl. Mater. Interfaces 13 (47) (2021) 56004–56013.
[19] J. Hansson, Q. Li, A. Smith, I. Zakaria, T. Nilsson, A. Nylander, L. Ye, P. Lundgren, J. Liu, P. Enoksson, Bipolar electrochemical capacitors using double-sided carbon nanotubes on graphite electrodes, J. Power Sources 451 (2020) 227765.
[20] R. Garg, S. Gonuguntla, S. Sk, M.S. Iqbal, A.O. Dada, U. Pal, M. Ahmadipour, Sputtering thin films: materials, applications, challenges and future directions, Adv. Colloid Interf. Sci. 330 (2024) 103203.
[21] D.R. Merrill, P.A. Tresco, Impedance characterization of microarray recording electrodes in vitro, IEEE Trans. Biomed. Eng. 52 (11) (2005) 1960–1965.
[22] C. Kleber, M. Bruns, K. Lienkamp, J. Rühe, M. Asplund, An interpenetrating, microstructurable and covalently attached conducting polymer hydrogel for neural interfaces, Acta Biomater. 58 (2017) 365–375.
[23] C. Boehler, F. Oberueber, S. Schlabach, T. Stieglitz, M. Asplund, Long-term stable adhesion for conducting polymers in biomedical applications: IrOx and nanostructured platinum solve the chronic challenge, ACS Appl. Mater. Interfaces 9 (1) (2017) 189–197.
[24] Y. Chen, J. Cai, Y. Huang, K. Lee, D. Tsai, Preparation and characterization of iridium dioxide–carbon nanotube nanocomposites for supercapacitors, Nanotechnology 22 (11) (2011) 115706.
[25] Y.-M. Chen, J.-H. Cai, Y.-S. Huang, K.-Y. Lee, D.-S. Tsai, K.-K. Tiong, A nanostructured electrode of IrOx foil on the carbon nanotubes for supercapacitors, Nanotechnology 22 (35) (2011) 355708.
[26] C. Zhong, Y. Deng, W. Hu, J. Qiao, L. Zhang, J. Zhang, A review of electrolyte materials and compositions for electrochemical supercapacitors, Chem. Soc. Rev. 44 (21) (2015) 7484–7539.
[27] P. Simon, Y. Gogotsi, Materials for electrochemical capacitors, Nat. Mater. 7 (11) (2008) 845–854.
[28] F. Béguin, V. Presser, A. Balducci, E. Frackowiak, Carbons and electrolytes for advanced supercapacitors, Adv. Mater. 26 (14) (2014) 2219–2251.
[29] Q. Abbas, P. Ratajczak, P. Babuchowska, A. Le Comte, D. Bélanger, T. Brousse, F. Béguin, Strategies to improve the performance of carbon/carbon capacitors in salt aqueous electrolytes, J. Electrochem. Soc. 162 (5) (2015) A5148.
[30] P. Kurzweil, M. Chwistek, Electrochemical stability of organic electrolytes in supercapacitors: spectroscopy and gas analysis of decomposition products, J. Power Sources 176 (2) (2008) 555–567.
[31] A. Brandt, S. Pohlmann, A. Varzi, A. Balducci, S. Passerini, Ionic liquids in supercapacitors, MRS Bull. 38 (07) (2013) 554–559.
[32] M. Haque, Q. Li, A.D. Smith, V. Kuzmenko, E. Köhler, P. Lundgren, P. Enoksson, Thermal influence on the electrochemical behavior of a supercapacitor containing an ionic liquid electrolyte, Electrochim. Acta 263 (2018) 249–260, https://doi.org/10.1016/j.electacta.2018.01.029.
[33] M. Haque, Q. Li, C. Rigato, A. Rajaras, A.D. Smith, P. Lundgren, P. Enoksson, Identification of self-discharge mechanisms of ionic liquid electrolyte based supercapacitor under high-temperature operation, J. Power Sources 485 (2021) 229328.
[34] R. Lin, P.-L. Taberna, S. Fantini, V. Presser, C.R. Pérez, F. Malbosc, N. L. Rupesinghe, K.B. Teo, Y. Gogotsi, P. Simon, Capacitive energy storage from− 50 to 100 c using an ionic liquid electrolyte, The Journal of Physical Chemistry Letters 2 (19) (2011) 2396–2401.
[35] B. Pal, S. Yang, S. Ramesh, V. Thangadurai, R. Jose, Electrolyte selection for supercapacitive devices: a critical review, Nanoscale Advances 1 (10) (2019) 3807–3835.
[36] S. Alipoori, S. Mazinani, S.H. Aboutalebi, F. Sharif, Review of PVA-based gel polymer electrolytes in flexible solid-state supercapacitors: opportunities and challenges, J. Energy Storage 27 (2020) 101072.
[37] H. Dai, G. Zhang, D. Rawach, C. Fu, C. Wang, X. Liu, M. Dubois, C. Lai, S. Sun, Polymer gel electrolytes for flexible supercapacitors: recent progress, challenges, and perspectives, Energy Storage Mater. (2020).
[38] J.H. Scofield, Hartree-slater subshell photoionization cross-sections at 1254 and 1487 eV, J. Electron Spectrosc. Relat. Phenom. 8 (2) (1976) 129–137.
[39] A.A. Wilson, M.B. Graziano, A.C. Leff, B. Hanrahan, D.R. Baker, M. Rivas, B. Sánchez, T. Parker, P. Sunal, Growth conditions and mechanisms for IrOx nano-platelet formation by reactive sputtering, J. Cryst. Growth 577 (2022) 126374.
[40] T. Mittmann, T. Szyjka, H. Alex, M.C. Istrate, P.D. Lomenzo, L. Baumgarten, M. Müller, J.L. Jones, L. Pintilie, T. Mikolajick, Impact of iridium oxide electrodes on the ferroelectric phase of thin hf0. 5Zr0. 5O2 films, Physica Status Solidi (RRL)–Rapid Research Letters 15 (5) (2021) 2100012.
[41] S.J. Freakley, J. Ruiz-Esquius, D.J. Morgan, The x-ray photoelectron spectra of ir, IrO2 and IrCl3 revisited, Surf. Interface Anal. 49 (8) (2017) 794–799.
[42] A.G. Shard, B.P. Reed, D.J. Cant, Surface analysis insight note: uncertainties in XPS elemental quantification, Surf. Interface Anal. 57 (6) (2025) 389–395.
[43] T.R. Gengenbach, G.H. Major, M.R. Linford, C.D. Easton, Practical guides for x-ray photoelectron spectroscopy (XPS): interpreting the carbon 1s spectrum, J. Vac. Sci. Technol. A 39 (1) (2021).
[44] Z. Novotny, B. Tobler, L. Artiglia, M. Fischer, M. Schreck, J.R. Raabe, J. R. Osterwalder, Kinetics of the thermal oxidation of ir (100) toward IrO2 studied by ambient-pressure x-ray photoelectron spectroscopy, The Journal of Physical Chemistry Letters 11 (9) (2020) 3601–3607.
[45] M. Li, J. Liu, Y. Xu, G. Qian, Phosphate adsorption on metal oxides and metal hydroxides: a comparative review, Environ. Rev. 24 (3) (2016) 319–332.
[46] M. Hayyan, F.S. Mjalli, M.A. Hashim, I.M. AlNashef, T.X. Mei, Investigating the electrochemical windows of ionic liquids, J. Ind. Eng. Chem. 19 (1) (2013) 106–112.
[47] M. Khademi, D.P. Barz, Structure of the electrical double layer revisited: electrode capacitance in aqueous solutions, Langmuir 36 (16) (2020) 4250–4260.
[48] A. Purwidyantri, T. Domingues, J. Borme, J.R. Guerreiro, A. Ipatov, C.M. Abreu, M. Martins, P. Alpuim, M. Prado, Influence of the electrolyte salt concentration on DNA detection with graphene transistors, Biosensors 11 (1) (2021) 24.
[49] C. Liang, R.R. Rao, K.L. Svane, J.H. Hadden, B. Moss, S.B. Scott, M. Sachs, J. Murawski, A.M. Frandsen, D.J. Riley, Unravelling the effects of active site density and energetics on the water oxidation activity of iridium oxides, Nat. Catal. 7 (7) (2024) 763–775.
[50] C. Liang, Y. Katayama, Y. Tao, A. Morinaga, B. Moss, V. Celorrio, M. Ryan, I. E. Stephens, J.R. Durrant, R.R. Rao, Role of electrolyte pH on water oxidation for iridium oxides, J. Am. Chem. Soc. 146 (13) (2024) 8928–8938.
[51] C. Spöri, J.T.H. Kwan, A. Bonakdarpour, D.P. Wilkinson, P. Strasser, The stability challenges of oxygen evolving catalysts: towards a common fundamental understanding and mitigation of catalyst degradation, Angew. Chem. Int. Ed. 56 (22) (2017) 5994–6021.
[52] S. Czioska, A. Boubnov, D. Escalera-López, J. Geppert, A. Zagalskaya, P. Röse, E. Saraçi, V. Alexandrov, U. Krewer, S. Cherevko, Increased Ir–Ir interaction in iridium oxide during the oxygen evolution reaction at high potentials probed by operando spectroscopy, ACS Catal. 11 (15) (2021) 10043–10057.
[53] N. De Vos, C. Maton, C.V. Stevens, Electrochemical stability of ionic liquids: general influences and degradation mechanisms, ChemElectroChem 1 (8) (2014) 1258–1270.
[54] M. Haque, Q. Li, A.D. Smith, V. Kuzmenko, P. Rudquist, P. Lundgren, P. Enoksson, Self-discharge and leakage current mitigation of neutral aqueous-based supercapacitor by means of liquid crystal additive, J. Power Sources 453 (2020) 227897.
[55] M. Armand, F. Endres, D.R. MacFarlane, H. Ohno, B. Scrosati, Ionic-liquid materials for the electrochemical challenges of the future, Nat. Mater. 8 (8) (2009) 621–629.
[56] M. Haque, I. Abdurrokhman, A. Idström, Q. Li, A. Rajaras, A. Martinelli, L. Evenäs, P. Lundgren, P. Enoksson, Exploiting low-grade waste heat to produce electricity through supercapacitor containing carbon electrodes and ionic liquid electrolytes, Electrochim. Acta 403 (2022) 139640.
[57] Q. Li, S. Sun, A.D. Smith, P. Lundgren, Y. Fu, P. Su, T. Xu, L. Ye, L. Sun, J. Liu, Compact and low loss electrochemical capacitors using a graphite/carbon nanotube hybrid material for miniaturized systems, J. Power Sources 412 (2019) 374–383.
[58] D.-Q. Liu, S.-H. Yu, S.-W. Son, S.-K. Joo, Electrochemical performance of iridium oxide thin film for supercapacitor prepared by radio frequency magnetron sputtering method, ECS Trans. 16 (1) (2008) 103.
[59] M. Borysiewicz, M. Wzorek, M. Kwoka, T. Wojciechowski, Vacuum-deposited thin film porous ZnO-metal oxide hybrid systems for microsupercapacitor applications with Ir/IrO2 in ZnO as a new, high-performance electrode, Nanotechnology 33 (2) (2021) 025405.
[60] A.A.F. Grupioni, E. Arashiro, T.A.F. Lassali, Voltammetric characterization of an iridium oxide-based system: the pseudocapacitive nature of the ir0. 3Mn0. 7O2 electrode, Electrochim. Acta 48 (4) (2002) 407–418.